Dual-band moiré metasurface patches for multifunctional biomedical applications†

Zilong Wu,[a] Glen Kelp,[b] Maruthi Nagavalli Yogeesh,[c] Wei Li,[c] Kyle M. McNicholas,[c] Andrew Briggs,[c] Bharath Bangalore Rajeeva,[a] Deji Akinwande,[c] Seth R. Bank,[c] Gennady Shvets[b] and Yuebing Zheng*[a]

There has been strong interest in developing multi-band plasmonic metasurfaces for multiple optical functions on single platforms. Herein, we developed Au moiré metasurface patches (AMMP), which leverage the tunable multi-band responses of Au moiré metasurfaces and the additional field enhancements of the metal–insulator–metal configuration to achieve dual-band plasmon resonance modes in near-infrared and mid-infrared regimes with high field enhancement. Furthermore, we demonstrate the multifunctional applications of AMMP, including surface-enhanced infrared spectroscopy, optical capture and patterning of bacteria, and photothermal denaturation of proteins. With their multiple functions of high performance, in combination with cost-effective fabrication using moiré nanosphere lithography, the AMMP will enable the development of highly integrated biophotonic platforms for a wide range of applications in disease theranostics, sterilization, and the study of microbiomes.

Introduction

Progress in biophotonics, an emerging field that applies photonic techniques to biological and medical research, relies on the development of new optically active materials that can measure, control and process biological cells and molecules at an unprecedented level.[1–8] Benefiting from the plasmon-enhanced local electromagnetic field and the associated photothermal effect at the rationally designed two-dimensional (2D) arrays of plasmonic nanostructures, plasmonic metasurfaces have shown promise for a variety of biomedical applications.[9–15] For example, enhanced light absorption by metal nanoparticles at surface plasmon resonances (SPRs) can convert efficiently the incident photon energy to thermal energy and heat the particle surfaces up to 200 °C,[16] which is promising for photothermal therapy of various medical conditions, including cancer.[17] The photothermal effect has also proven to be efficient in thermal denaturation of proteins for food processing.[18] The enhanced electromagnetic field at plasmonic metasurfaces underpins their use in surface-enhanced optical spectroscopy for biology and medicine. In particular, surface-enhanced infrared spectroscopy (SEIRS) is capable of sensitive and label-free detection of biomedical analytes such as lipids, proteins, and nucleic acids.[19,20] The strongly enhanced electromagnetic field at plasmonic metasurfaces increases the intrinsically weak vibrational infrared (IR) absorption of the biomolecules in SEIRS.[10,11]

One of the trends in plasmonic metasurfaces for biomedical applications is to integrate multiple functions such as optical sensing and photothermal heating on single platforms.[21–24] Multifunctional integration offers several advantages, including miniaturized devices and real-time therapeutic monitoring. However, most of the current plasmonic metasurfaces that exhibit single-band plasmon resonances cannot meet the requirements of the single-platform multifunctional integration because different biomedical applications require different working wavelengths for their optimal performances. For example, plasmonic resonances at near-infrared (NIR) within biological windows (650 nm to 900 nm and 1000 nm to 1400 nm)[1,25] are required for optimal in vivo photothermal therapy, while mid-infrared (MIR) light with wavelengths of >3 μm is needed to match the IR vibrational absorption bands of biomolecules in SEIRS. Therefore, multiband plasmonic metasurfaces where different bands give the best performances for different biomedical functions are highly desired for the integrated multi-functional applications based on single material platforms.

[a] Department of Mechanical Engineering, Materials Science and Engineering Program, and Texas Materials Institute, The University of Texas at Austin, Austin, Texas 78712, USA. E-mail: zheng@austin.utexas.edu
[b] Department of Physics, The University of Texas at Austin, Austin, Texas 78712, USA
[c] Microelectronics Research Centre, The University of Texas at Austin, Austin, Texas 78758, USA

Moiré metasurfaces,[26,27] which feature plasmonic nanostructures with variable sizes and shapes in 2D moiré patterns, support multiple surface plasmon modes that lead to multiband optical responses covering large segments of the electromagnetic spectrum.[28,29] Using a directed-assembly method known as moiré nanosphere lithography (MNSL), we can fabricate the moiré metasurfaces in a high-throughput and cost-effective manner.[30] We have demonstrated that Au moiré metasurfaces support multiple surface plasmon resonances that span working wavelengths from visible to MIR regimes for both photothermal and sensing applications.[28] By controlling the moiré pattern and plasmonic nanostructure geometry, one should be able to finely tune the multi-band optical responses for the different applications with optimal performances.[28] However, the large variety of plasmonic nanostructures in the 2D arrays results in weak optical responses from each type of surface plasmon mode because only a small percentage of the nanostructures supports the specific types of modes. The weak optical responses have significantly limited multifunctional biomedical applications of current moiré metasurfaces.

Herein, we develop a general strategy to improve the multi-band optical responses of moiré metasurfaces based on the metal–insulator–metal (MIM) structure. Known as the moiré metasurface patch, our MIM structure is composed of a moiré metasurface and an optically thick metal film with a dielectric spacer layer sandwiched between them. The multiple light reflections between the moiré metasurface and the metal film enhance the surface plasmon resonances at the metasurface. Using Au moiré metasurfaces as examples, we demonstrate Au moiré metasurface patches (AMMP) that exhibit strongly enhanced dual-band plasmon resonances in the NIR (~1300 nm) and MIR (~5 μm) regimes. Furthermore, we demonstrate the use of the dual-band AMMP for multifunctional biomedical applications. Our single-platform applications include: (1) SEIRS of an ultrathin layer of poly(methyl methacrylate) (PMMA) and proteins; (2) optical capture and immobilization of bacteria based on the plasmon-enhanced generation of microbubbles; and (3) plasmon-enhanced photothermal denaturation and spectroscopic analysis of proteins.

Fabrication and characterization of moiré metasurface patches

Fig. 1(a) shows a schematic of the AMMP structure, where a MgF$_2$ dielectric layer is sandwiched between an Au moiré metasurface and an Au film on a glass substrate. The fabrication process is illustrated in Fig. S1.† The thicknesses of the Au moiré metasurface, MgF$_2$ layer and Au film were 20 nm, 300 nm and 100 nm, respectively. We fabricated the Au moiré metasurfaces using MNSL, where the moiré pattern and plasmonic nanostructure geometry were precisely tuned to obtain plasmonic resonances that are suitable for photothermal heating and MIR sensing applications (Fig. S2†).[28,30] Fig. 1(b) shows a scanning electron micrograph of the Au moiré metasurface of the AMMP. The moiré metasurface included three
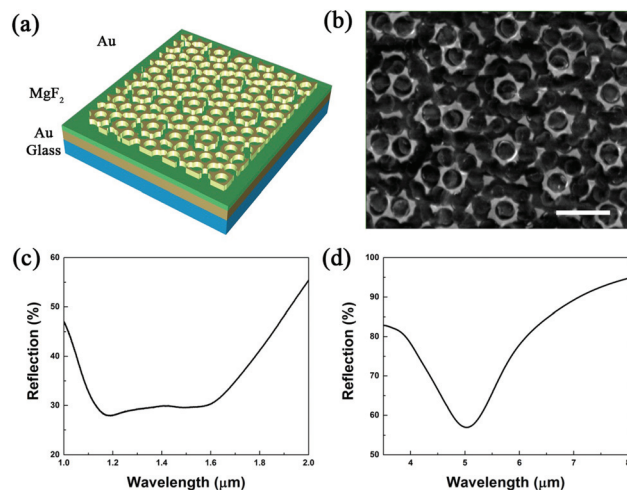

Fig. 1 (a) Schematic of AMMP. (b) Scanning electron micrograph of an Au moiré metasurface of the AMMP. The scale bar is 2 μm. (c) Reflection spectrum of an AMMP in the NIR regime. (d) Reflection spectrum of an AMMP in the MIR regime.

types of Au nanostructures: the ring-like nanostructures, the z-shaped nanostructures, and the triangular nanostructures. The inner and outer diameters of the ring-like structures were ~700 nm and ~900 nm, respectively. The z-shaped structures had a length of ~800 nm and the triangular structures had an edge of ~320 nm.

With the different types of plasmonic nanostructures in the metasurfaces,[31] the AMMP can support multiple surface plasmon resonances at various wavelength regimes. Fig. 1(c) and (d) show the measured reflection spectra from the AMMP in air at the NIR (0.7–2 μm) and MIR (3–8 μm) regimes, respectively. As shown in Fig. 1(c), the AMMP had a low reflection of ~30% from ~1.1 μm to ~1.6 μm. The low reflection indicates a high absorption of incident light by the AMMP since the optically thick Au layer of 100 nm blocks the light transmission. The broad absorption is attributed to the excitation of plasmon resonances of the z-shaped and triangular nanostructures of variable sizes. In the reflection spectrum of Fig. 1(d), we attribute the dip at the wavelength of ~5 μm to the excitation of plasmon resonances of the ring-like nanostructures, revealing an efficient MIR light absorption by the AMMP. With the strong optical responses in the NIR and MIR regimes, the AMMP are promising for multiple biomedical applications such as photothermal heating and IR sensing. Compared with other reported dual-band metasurfaces that rely on costly and low-throughput electron-beam lithography, the AMMP provide cost-effective and scalable substrates for biomedical applications. In addition, as shown in Fig. 1(c), the broadband absorption in the NIR regime enables the high versatility in choosing working lasers with wavelengths from 1.2 to 1.6 μm for the photothermal treatment. It is worth mentioning that the uniformity of the AMMP can be improved by using nanosphere monolayers with large single-crystalline domains in MNSL.[32] The

uniformity improvement of the metasurfaces can lead to the higher optical absorption efficiency and the higher performances in biomedical applications.

The optical responses of the AMMP, as shown in Fig. 1(c) and (d), arise from the combined effects of the Au moiré metasurface and the MIM structure. We employed optical simulations based on finite-difference time-domain (FDTD) methods to evaluate the enhancements of the optical responses by the MIM configuration. Fig. 2(a) shows the simulated NIR absorption spectra of an Au moiré metasurface with and without the MIM configuration in air. For the Au moiré metasurfaces without the MIM configuration, there is weak and broad optical absorption from ~1.0 μm to ~1.8 μm. The broad optical absorption arises from surface plasmon resonances of triangular and z-shaped nanostructures. Fig. S3† shows the simulated absorption spectra of the two representative nanostructures along with electric field distributions at the resonance wavelengths. In total, three resonance modes at different peak wavelengths are excited in the NIR regime. The average effects from many triangular and z-shape nanostructures with slightly variable shapes and sizes lead to the weak and broad optical absorption of the moiré metasurfaces. The Au moiré metasurface with the MIM configuration (or AMMP) exhibits a significantly enhanced light absorption in the same wavelength regime. The line shape of the simulated absorption spectrum of the AMMP is consistent with the measured reflection spectrum in Fig. 1(c). We explain the absorption enhancement in the MIM configuration based on a multiple reflection model. As illustrated by the schematic in the inset of Fig. 2(a), the incident light is partially reflected and transmitted into the spacer layer through the Au moiré metasurface. The transmitted light propagates in the spacer and can be reflected by the Au film, leading to multiple reflections between the Au moiré metasurface and the Au film. The

multiple reflections significantly increase the light absorption by the Au moiré metasurface at the plasmon resonances.

Fig. 2(b) plots the simulated MIR absorption spectra of the Au moiré metasurface with and without the MIM configuration in air, which exhibited dipole plasmon resonances of the ring-like nanostructure. The MIM configuration caused a red shift of the absorption peak from ~3.7 μm to ~5 μm. The insets of Fig. 2(b) show the simulated distributions of electric field intensity at the ring-like structures with and without the MIM configuration. The wavelengths used for the field-distribution simulations were 3560 nm and 4960 nm, respectively. We can see that the MIM configuration further increased the plasmon-enhanced electromagnetic fields at the ring-like structure in air. The field enhancement makes the AMMP a better candidate than the Au moiré metasurface for SEIRS, where the sensitivity is proportional to the square of the electric-field amplitude at the analytes.[33]

The MIM configuration impacts differently the absorption spectra of the metasurfaces in the NIR and MIR regimes due to the different coupling effects. In the MIR regime, the optical absorption of the AMMP arises from localized surface plasmon resonances of ring-like nanostructures, as shown in Fig. 2(b). With the MIM configuration, the multiple reflections in the spacer lead to a near-field interaction between the ring-like nanostructure and its image in the Au film, which is known as out-of-plane coupling.[34] The out-of-plane coupling causes a redshift in the resonance wavelength of the nanostructure.[34,35]

In the NIR regime, the multiple reflections in the spacer can also induce electromagnetic coupling between the Au moiré metasurfaces and the Au film in the MIM configuration. The smaller nanostructures such as triangular nanostructures in the moiré metasurfaces support surface plasmon modes in the NIR regime. These dense and gradient NIR-active nanostructures in the moiré metasurfaces can be considered as an effective continuous thin film.[36] In this case, the absorption peak wavelength of the AMMP makes a blueshift and then a redshift when the MIM configuration is introduced and the spacer thickness is increased. The increased spacer thickness also enhances the absorption intensity and bandwidth.[36] Therefore, the introduction of the MIM configuration with a thick spacer (300 nm) into the Au moiré metasurface increases the absorption bandwidth and intensity in the NIR regime, as shown in Fig. 2(a).

Fig. S4† compares the electric-field distributions at the bottom surfaces of the Au moiré metasurfaces with and without the MIM configuration. The simulations were carried out for both NIR and MIR regimes. We can see that the enhanced electric field in the MIR regime is concentrated near the ring-like nanostructures in the AMMP, revealing the occurrence of the coupling between individual ring-like nanostructures and the Au film. In contrast, the enhanced electric field in the NIR regime occurs both near the Au nanostructures and at the empty area in the AMMP. The global field distribution confirms that the Au moiré metasurface interacts with the Au film as an effective continuous film.
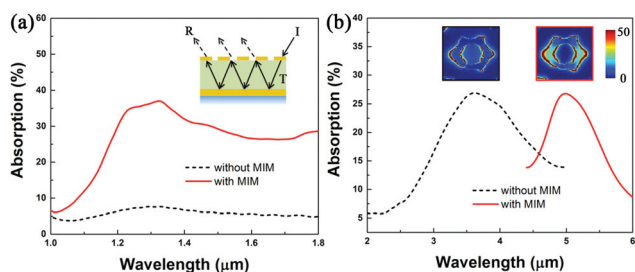

Fig. 2 (a) Simulated NIR absorption spectra of the Au moiré metasurface with and without the MIM configuration in air. The inset is the schematic illustration of the multiple reflections of light in the spacer layer that enhance the light absorption by the metasurface. I, T and R depict the incident, transmitted and reflected light, respectively. (b) Simulated MIR absorption spectra of the Au moiré metasurface with and without the MIM configuration. The insets show the electric-field intensity distributions (when excited at the peak wavelengths) at the ring-like nanostructure with and without the MIM configuration. The white dashed lines in the insets depict the inner boundaries of the ring-like structures.

Surface-enhanced infrared spectroscopy

In a typical SEIRS, surface plasmons can couple with molecular vibrations where there is an overlap between the absorption spectra of plasmonic substrates and molecules,[37] enhancing the molecular vibrational signals as additional peaks or dips in the extinction (or reflection) spectra of the substrates.[9,38] We demonstrate the AMMP-based SEIRS in the MIR regime for detection of the thin layers of PMMA and proteins, *i.e.*, bovine serum albumin (BSA). As shown in Fig. 3(a), a thin layer of PMMA (~20 nm) caused two prominent changes in the reflection spectrum of AMMP. One is a red shift in the reflection dip (*i.e.*, from ~5 μm to ~5.25 μm) due to the increased refractive index of the AMMP surrounding. The refractive index sensitivity was 510 nm per RIU (refractive index units), despite the nanometric thickness of the PMMA layer. The other was the emergence of an additional dip at ~5.8 μm in the reflection spectrum, which is attributed to the vibrational mode of the acrylate carboxyl group in PMMA.[39] A small dip at ~5.7 μm was observed in the reflection spectrum from an Au thin film coated with PMMA of the same thickness. The coupling between the vibrational modes of PMMA and the plasmonic modes leads to a slight modification in the line shape and spectral shift in the reflection dip.[40,41] The AMMP-based SEIRS features a significantly enhanced molecular vibrational signal with the peak-to-dip difference (~10%) ten times higher than the Au film (~1%).

Fig. 3(b) compares the MIR absorbance spectra of BSA on the AMMP and the Au film. The BSA molecules were physically adsorbed on the surfaces of the AMMP and Au film as sub-monolayers. The absorbance spectra were derived from the reflection spectra of the substrates with and without BSA as $-\log(R_{BSA}/R_0)$, where R_{BSA} and R_0 are the reflections of the AMMP with and without BSA, respectively. Two resonant peaks appeared in the absorbance spectrum of AMMP with BSA. The two peaks are attributed to the C=O stretching and N–H bending modes in the amide functional group of BSA, as illus-

trated in the inset of Fig. 3(b). In contrast, the absorbance spectrum of the Au film with BSA is featureless, revealing no information on the BSA. The enhancement (>10 times) in the molecular signals is comparable to that of SEIRS substrates based on perfect absorbers.[42] The comparative study indicates that AMMP can be an excellent platform for SEIRS in molecular analysis.

Optical capture and immobilization of bacteria

The capability of capturing bacteria from solutions and immobilizing them in designed patterns on substrates can benefit sterilization and the study of microbiomes.[43–48] Inspired by our recent demonstration of bubble-pen lithography,[49] we explored plasmon-induced microbubbles to capture and pattern bacteria on AMMP. We employed a NIR laser beam with a wavelength of 1310 nm to generate microbubbles on the AMMP (Fig. 4a). As shown in Fig. 1(c), our AMMP had strong optical absorption at 1310 nm due to the plasmon resonances, leading to the further enhancement of the photothermal effects of the NIR light. It is worth mentioning that our AMMP allow the use of variable NIR lasers with wavelengths from 1.2 to 1.6 μm due to the broadband absorption in the NIR regime, as shown in Fig. 1(c). As illustrated in Fig. 4(b)–(e), upon the laser irradiation at the interface of AMMP and aqueous solution (*i.e.*, DI water), the plasmon-enhanced photothermal heating[50,51] generated a microbubble at the AMMP surface, which captured *E. coli* bacteria suspended in the solution and immobilized them on the AMMP. Specifically, a laser beam with a spot size of ~4 μm was focused on the AMMP (Fig. 4c). When the power intensity was increased to 0.4 mW μm⁻², a microbubble was generated at the beam site on the AMMP (Fig. 4d) due to water vaporization from photothermal effects that are enhanced by the plasmonic modes. In contrast, a much larger power of a few tens of mW μm⁻² was needed to generate microbubbles on Au thin films.[52] This power intensity is also lower than the value for generating microbubbles on quasi-continuous Au nanoislands.[49] Upon the generation of the microbubble, *E. coli* bacteria suspended in the solution were captured onto the bubble surface *via* the combined effects of Marangoni convection, surface tension, and gas pressure.[49] Once the laser beam was turned off, the microbubble disappeared and the captured bacteria were immobilized onto the AMMP surface as a cluster (Fig. 4e). The number of the bacteria in the cluster can be controlled by the "ON" time of the laser beam (or microbubble) and the concentration of bacteria in the solution. It is worth mentioning that the bubble generation is independent of the position of the laser spot relative to the Au nanostructures on the AMMP surface. The diameter of the laser spot (~4 μm) is larger than the quasi-period of the moiré pattern (~2 μm, as shown in Fig. 1b). Thus, independent of the position of the laser spot on the AMMP surface, a similar number (~4 quasiperiodic units) of
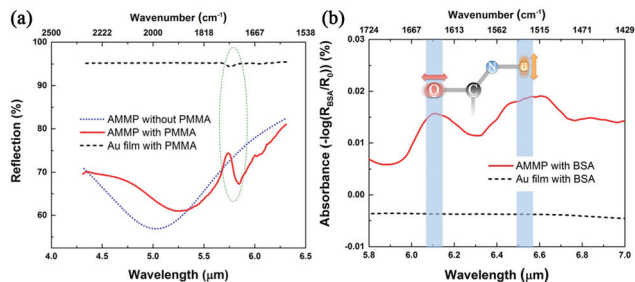
Fig. 3 (a) Reflection spectra of the AMMP with and without PMMA, as well as an Au film with PMMA. The green dashed ellipse marks the dips that arise from the same molecular vibrational mode. (b) MIR absorbance spectra of BSA on the AMMP and Au film, which are the differences between the reflection spectra of the substrates with and without BSA. The spectra are vertically offset for clarity. The schematic in the inset illustrates the corresponding vibrational modes of BSA.
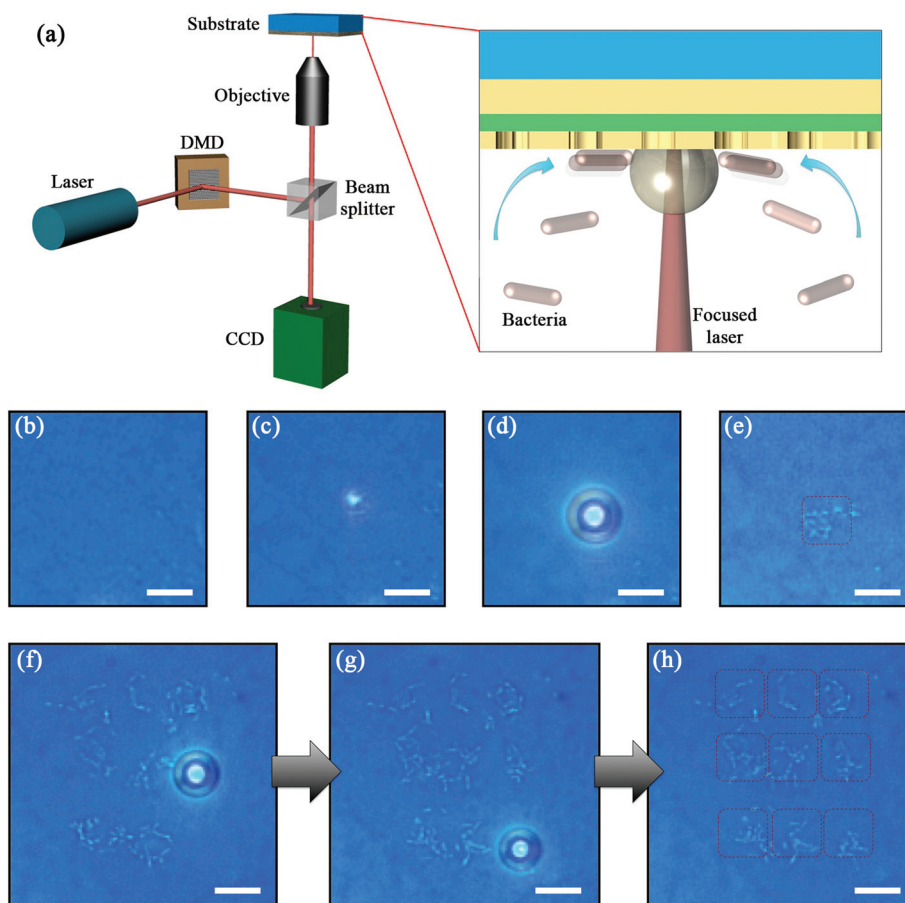
Fig. 4 (a) Schematic of our experimental setup for capture and immobilization of bacteria on the AMMP using plasmon-induced microbubbles. The inset shows the cross-sectional view of the transport and trapping of the bacteria at a microbubble generated by a laser beam at the interface of the AMMP and solution. (b) Optical images of the AMMP substrate immersed in the *E. coli* solution. (c) Optical image of AMMP irradiated by a NIR laser beam. (d) Optical image of a microbubble generated at the laser spot on the AMMP surface. (e) Optical image of *E. coli* cells immobilized on the AMMP after the disappearance of the bubble. (f–h) Time-evolved optical images show the microbubble-based patterning of the 3 × 3 array of *E. coli* clusters (indicated by dashed squares) on the AMMP substrate. The patterning is from top to bottom and from left to right. The scale bars are 10 μm.

Au nanostructures is excited to generate microbubbles *via* the photothermal effect.

Steering the laser beam allows us to create patterns of the multiple bacteria clusters on the AMMP (Fig. S5†). As an example, Fig. 4(f)–(h) demonstrate the patterning of *E. coli* clusters into a 3 × 3 array on the AMMP surface. We used a digital micromirror device (DMD) to control the laser beam for the microbubble-based patterning. The patterning occurred from top to bottom and from left to right. For each *E. coli* cluster, a microbubble was maintained for 1 minute, leading to the cluster with a lateral size of ~6 μm. The laser beam was temporarily turned off when being moved to the next spot, where a new microbubble was generated for the capture and immobilization of bacteria on the AMMP when the laser was turned on again. The process was repeated to create the targeted patterns of the bacteria clusters, as shown in Fig. 4(h).

The optical capturing of bacterial cells can be an effective approach for water sterilization. Compared with other sterilization methods based on photothermal effects, which require

pre-deposition of bacteria on plasmonic substrates or plasmonic nanoparticles suspended in water, our microbubble-based method is simpler and greener. In addition, our capability of patterning bacteria in designed patterns will enable the further study of microbiomes using SEIRS and other characterization tools.

Photothermal denaturation and spectroscopic analysis of proteins

Denaturation of proteins through the plasmonic heating effect has proven effective for cell inactivation applications.[16,18] Conventional characterization methods such as FTIR and fluorescence spectroscopies for the denaturation process require a large amount of samples[17] or fluorescent labeling chemistry of proteins.[16] Herein, with their significantly enhanced dual-band optical responses in NIR and MIR regimes, AMMP have been applied for both photothermal denaturation and label-
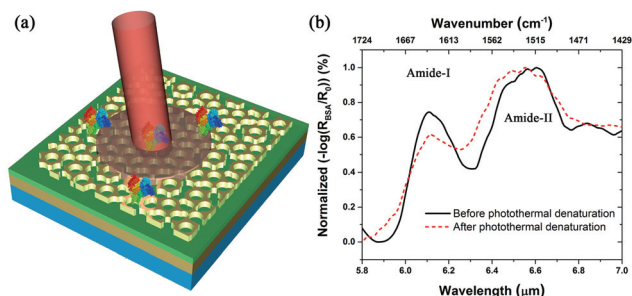
Fig. 5 (a) Schematic of the plasmon-enhanced photothermal denaturation of BSA on AMMP using a NIR laser. (b) Spectroscopic analysis of the photothermal denaturation of BSA on AMMP using SEIRS in the MIR regime.

free spectroscopic analysis of a small amount of proteins on the single substrates. Fig. 5(a) shows the schematic of the plasmon-enhanced photothermal denaturation of BSA on an AMMP. The sample was immersed in DI water to improve the protein denaturation.[53] We expanded the 1310 nm laser beam to a diameter of ~20 μm and focused it at the interface of the AMMP and water. The plasmon-enhanced heating can increase the temperature inside the laser spot to 80 °C and beyond, which is high enough for denaturation of BSA.[53] The laser irradiation of the samples lasted for 10 minutes.[53]

Taking advantage of the dual-band optical responses of the AMMP, we applied SEIRS in the MIR regime to analyze the photothermal denaturation of BSA on the same substrates. A FTIR spectrometer integrated with an IR microscope was employed for the SEIRS of the BSA under the photothermal treatment. Fig. 5(b) shows the absorbance spectra of the BSA on AMMP before and after the photothermal heating with the NIR laser beam. The laser irradiation caused obvious changes in both amide-I and amide-II bands. Specifically, the intensity of the amide-I band decreased and the peak wavelength of the amide-II band made a blue shift after the photothermal heating. Consistent with the previous study, both types of spectral changes indicate the denaturation of BSA, which can lead to the tertiary conformational changes, the formation of β-aggregates and the secondary structural changes.[54] Since thermal denaturation of proteins is highly related to food science, heat-induced cell death, and cancer therapies,[18] our AMMP that provide photothermal treatment with *in situ* molecular characterization are promising as an integrated biomedical platform for both scientific research and clinical applications.

Conclusion

We have shown that combining an Au plasmonic moiré metasurface with the MIM configuration can achieve the dual-band AMMP with high field enhancements and plasmon resonance tunability in NIR and MIR regimes. Large-scale AMMP can be fabricated by MNSL in a cost-effective and high-efficient

manner. Our experimental studies of the AMMP are closely coupled to optical simulations. Based on our understanding of the optical properties and the associated photothermal effect of the AMMP, we have further demonstrated the applications of AMMP in multiple biomedical areas, including SEIRS for label-free analysis of PMMA and BSA, optical capture and patterning of bacteria, and photothermal denaturation and spectroscopic analysis of proteins. These demonstrations reveal that the AMMP are instrumental in serving as multifunctional biomedical platforms for both scientific research and clinical applications. With further improvement in their uniformity *via* the optimization of MNSL, the AMMP are expected to lead to commercially available biomedical products.[32]

Conflict of interest

The authors declare no competing financial interest.

Contributions

Z. W. and Y. Z. conceived the idea. Z. W., M. N. Y., and W. L. fabricated the samples. Z. W., B. B. R., G. K., K. M. M., and A. B. performed optical characterization and analyzed the data. Z. W. conducted the bacteria patterning and laser heating experiments. Z. W. conducted the optical simulations. D. A., S. R. B., G. S. and Y. Z. supervised the project. All authors contributed to writing of the manuscript.

Acknowledgements

References

1 Y. Jin, Engineering plasmonic gold nanostructures and metamaterials for biosensing and nanomedicine, *Adv. Mater.*, 2012, **24**, 5153–5165.

2 D. G. Grier, A revolution in optical manipulation, *Nature*, 2003, **424**, 810–816.

3 P. J. Pauzauskie, A. Radenovic, E. Trepagnier, H. Shroff, P. Yang and J. Liphardt, Optical trapping and integration of semiconductor nanowire assemblies in water, *Nat. Mater.*, 2006, **5**, 97–101.

4 Y. Cui, K. H. Fung, J. Xu, S. He and N. X. Fang, Multiband plasmonic absorber based on transverse phase resonances, *Opt. Express*, 2012, **20**, 17552–17559.

5 C. Zhao, Y. Liu, J. Yang and J. Zhang, Single-molecule detection and radiation control in solutions at high concentrations via a heterogeneous optical slot antenna, *Nanoscale*, 2014, **6**, 9103–9109.

6 C. Zhao, Y. Liu, Y. Zhao, N. Fang and T. J. Huang, A reconfigurable plasmofluidic lens, *Nat. Commun.*, 2013, **4**, 2305.

7 Y. Shen, J. Zhou, T. Liu, Y. Tao, R. Jiang, M. Liu, G. Xiao, J. Zhu, Z.-K. Zhou, X. Wang, C. Jin and J. Wang, Plasmonic gold mushroom arrays with refractive index sensing figures of merit approaching the theoretical limit, *Nat. Commun.*, 2013, **4**, 2381.

8 L. Shao, Q. Ruan, R. Jiang and J. Wang, Macroscale colloidal noble metal nanocrystal arrays and their refractive index-based sensing characteristics, *Small*, 2014, **10**, 802–811.

9 B. Cerjan, X. Yang, P. Nordlander and N. J. Halas, Asymmetric aluminum antennas for self-calibrating surface-enhanced infrared absorption spectroscopy, *ACS Photonics*, 2016, **3**, 354–360.

10 C. D'Andrea, J. Bochterle, A. Toma, C. Huck, F. Neubrech, E. Messina, B. Fazio, O. M. Maragò, E. Di Fabrizio, M. Lamy de La Chapelle, P. G. Gucciardi and A. Pucci, Optical nanoantennas for multiband surface-enhanced infrared and raman spectroscopy, *ACS Nano*, 2013, **7**, 3522–3531.

11 H. Aouani, H. Šípová, M. Rahmani, M. Navarro-Cia, K. Hegnerová, J. Homola, M. Hong and S. A. Maier, Ultrasensitive broadband probing of molecular vibrational modes with multifrequency optical antennas, *ACS Nano*, 2013, **7**, 669–675.

12 V. Flauraud, T. S. van Zanten, M. Mivelle, C. Manzo, M. F. Garcia Parajo and J. Brugger, Large-scale arrays of bowtie nanoaperture antennas for nanoscale dynamics in living cell membranes, *Nano Lett.*, 2015, **15**, 4176–4182.

13 N. Zhang, K. Liu, Z. Liu, H. Song, X. Zeng, D. Ji, A. Cheney, S. Jiang and Q. Gan, Ultrabroadband metasurface for efficient light trapping and localization: A universal surface-enhanced raman spectroscopy substrate for "all" excitation wavelengths, *Adv. Mater. Interfaces*, 2015, **2**, 1500142.

14 Z. Wu and Y. Zheng, Radiative enhancement of plasmonic nanopatch antennas, *Plasmonics*, 2015, **11**, 1–10.

15 Y. Liu and X. Zhang, Metasurfaces for manipulating surface plasmons, *Appl. Phys. Lett.*, 2013, **103**, 141101.

16 G. M. Santos, F. I. D. Ferrara, F. S. Zhao, D. F. Rodrigues and W. C. Shih, Photothermal inactivation of heat-resistant bacteria on nanoporous gold disk arrays, *Opt. Mater. Express*, 2016, **6**, 1217–1229.

17 Z. Meng, F. Wei, R. Wang, M. Xia, Z. Chen, H. Wang and M. Zhu, NIR-laser-switched in vivo smart nanocapsules for synergic photothermal and chemotherapy of tumors, *Adv. Mater.*, 2016, **28**, 245–253.

18 Z. Qin, S. K. Balasubramanian, W. F. Wolkers, J. A. Pearce and J. C. Bischof, Correlated parameter fit of arrhenius model for thermal denaturation of proteins and cells, *Ann. Biomed. Eng.*, 2014, **42**, 2392–2404.

19 O. Limaj, D. Etezadi, N. J. Wittenberg, D. Rodrigo, D. Yoo, S. H. Oh and H. Altug, Infrared plasmonic biosensor for real-time and label-free monitoring of lipid membranes, *Nano Lett.*, 2016, **16**, 1502–1508.

20 C. Wu, A. B. Khanikaev, R. Adato, N. Arju, A. A. Yanik, H. Altug and G. Shvets, Fano-resonant asymmetric metamaterials for ultrasensitive spectroscopy and identification of molecular monolayers, *Nat. Mater.*, 2012, **11**, 69–75.

21 J. M. Tam, J. O. Tam, A. Murthy, D. R. Ingram, L. L. Ma, K. Travis, K. P. Johnston and K. V. Sokolov, Controlled assembly of biodegradable plasmonic nanoclusters for near-infrared imaging and therapeutic applications, *ACS Nano*, 2010, **4**, 2178–2184.

22 X. Huang, I. H. El-Sayed, W. Qian and M. A. El-Sayed, Cancer cell imaging and photothermal therapy in the near-infrared region by using gold nanorods, *J. Am. Chem. Soc.*, 2006, **128**, 2115–2120.

23 T. Vo-Dinh, A. M. Fales, G. D. Griffin, C. G. Khoury, Y. Liu, H. Ngo, S. J. Norton, J. K. Register, H.-N. Wang and H. Yuan, Plasmonic nanoprobes: From chemical sensing to medical diagnostics and therapy, *Nanoscale*, 2013, **5**, 10127–10140.

24 G. Q. Wallace, M. Tabatabaei, R. Hou, M. J. Coady, P. R. Norton, T. S. Simpson, S. M. Rosendahl, A. Merlen and F. Lagugné-Labarthet, Superimposed arrays of nanoprisms for multispectral molecular plasmonics, *ACS Photonics*, 2016, DOI: 10.1021/acsphotonics.1026b00388.

25 Y. Nakane, Y. Tsukasaki, T. Sakata, H. Yasuda and T. Jin, Aqueous synthesis of glutathione-coated PbS quantum dots with tunable emission for non-invasive fluorescence imaging in the second near-infrared biological window (1000–1400 nm), *Chem. Commun.*, 2013, **49**, 7584–7586.

26 J. H. Han, I. Kim, J. W. Ryu, J. Kim, J. H. Cho, G. S. Yim, H. S. Park, B. Min and M. Choi, Rotationally reconfigurable metamaterials based on moire phenomenon, *Opt. Express*, 2015, **23**, 17443–17449.

27 S. Ohno, Projection of phase singularities in moiré fringe onto a light field, *Appl. Phys. Lett.*, 2016, **108**, 251104.

28 Z. Wu, K. Chen, R. Menz, T. Nagao and Y. Zheng, Tunable multiband metasurfaces by moire nanosphere lithography, *Nanoscale*, 2015, **7**, 20391–20396.

29 S. M. Lubin, A. J. Hryn, M. D. Huntington, C. J. Engel and T. W. Odom, Quasiperiodic moiré plasmonic crystals, *ACS Nano*, 2013, **7**, 11035–11042.

30 K. Chen, B. B. Rajeeva, Z. Wu, M. Rukavina, T. D. Dao, S. Ishii, M. Aono, T. Nagao and Y. Zheng, Moiré nanosphere lithography, *ACS Nano*, 2015, **9**, 6031–6040.

31 Y. Cui, J. Xu, K. Hung Fung, Y. Jin, A. Kumar, S. He and N. X. Fang, A thin film broadband absorber based on multi-sized nanoantennas, *Appl. Phys. Lett.*, 2011, **99**, 253101.

32 E. Sirotkin, J. D. Apweiler and F. Y. Ogrin, Macroscopic ordering of polystyrene carboxylate-modified nanospheres self-assembled at the water-air interface, *Langmuir*, 2010, **26**, 10677–10683.

33 F. Le, D. W. Brandl, Y. A. Urzhumov, H. Wang, J. Kundu, N. J. Halas, J. Aizpurua and P. Nordlander, Metallic nanoparticle arrays: A common substrate for both surface-enhanced raman scattering and surface-enhanced infrared absorption, *ACS Nano*, 2008, **2**, 707–718.

34 L. Lin and Y. Zheng, Optimizing plasmonic nanoantennas via coordinated multiple coupling, *Sci. Rep.*, 2015, **5**, 14788.

35 H.-T. Chen, Interference theory of metamaterial perfect absorbers, *Opt. Express*, 2012, **20**, 7165–7172.

36 N. Zhang, Z. Dong, D. Ji, H. Song, X. Zeng, Z. Liu, S. Jiang, Y. Xu, A. Bernussi, W. Li and Q. Gan, Reversibly tunable coupled and decoupled super absorbing structures, *Appl. Phys. Lett.*, 2016, **108**, 091105.

37 R. Adato, A. Artar, S. Erramilli and H. Altug, Engineered absorption enhancement and induced transparency in coupled molecular and plasmonic resonator systems, *Nano Lett.*, 2013, **13**, 2584–2591.

38 D. Rodrigo, O. Limaj, D. Janner, D. Etezadi, F. J. García de Abajo, V. Pruneri and H. Altug, Mid-infrared plasmonic biosensing with graphene, *Science*, 2015, **349**, 165–168.

39 G. Duan, C. Zhang, A. Li, X. Yang, L. Lu and X. Wang, Preparation and characterization of mesoporous zirconia made by using a poly (methyl methacrylate) template, *Nanoscale Res. Lett.*, 2008, **3**, 118–122.

40 G. A. Wurtz, P. R. Evans, W. Hendren, R. Atkinson, W. Dickson, R. J. Pollard, A. V. Zayats, W. Harrison and C. Bower, Molecular plasmonics with tunable exciton–plasmon coupling strength in j-aggregate hybridized Au nanorod assemblies, *Nano Lett.*, 2007, **7**, 1297–1303.

41 F. Neubrech, A. Pucci, T. W. Cornelius, S. Karim, A. Garcia-Etxarri and J. Aizpurua, Resonant plasmonic and vibrational coupling in a tailored nanoantenna for infrared detection, *Phys. Rev. Lett.*, 2008, **101**, 157403.

42 K. Chen, T. D. Dao, S. Ishii, M. Aono and T. Nagao, Infrared aluminum metamaterial perfect absorbers for plasmon-enhanced infrared spectroscopy, *Adv. Funct. Mater.*, 2015, **25**, 6637–6643.

43 R. S. Norman, J. W. Stone, A. Gole, C. J. Murphy and T. L. Sabo-Attwood, Targeted photothermal lysis of the pathogenic bacteria, pseudomonas aeruginosa, with gold nanorods, *Nano Lett.*, 2008, **8**, 302–306.

44 W.-C. Huang, P.-J. Tsai and Y.-C. Chen, Functional gold nanoparticles as photothermal agents for selective-killing of pathogenic bacteria, *Nanomedicine*, 2007, **2**, 777–787.

45 Y. Zhao and X. Jiang, Multiple strategies to activate gold nanoparticles as antibiotics, *Nanoscale*, 2013, **5**, 8340–8350.

46 P. S. Weiss, Opportunities for nanoscience and nanotechnology in studying microbiomes, *ACS Nano*, 2016, **10**, 1–2.

47 J. S. Biteen, P. C. Blainey, Z. G. Cardon, M. Chun, G. M. Church, P. C. Dorrestein, S. E. Fraser, J. A. Gilbert, J. K. Jansson, R. Knight, J. F. Miller, A. Ozcan, K. A. Prather, S. R. Quake, E. G. Ruby, P. A. Silver, S. Taha, G. van den Engh, P. S. Weiss, G. C. L. Wong, A. T. Wright and T. D. Young, Tools for the microbiome: Nano and beyond, *ACS Nano*, 2016, **10**, 6–37.

48 A. P. Alivisatos, M. J. Blaser, E. L. Brodie, M. Chun, J. L. Dangl, T. J. Donohue, P. C. Dorrestein, J. A. Gilbert, J. L. Green, J. K. Jansson, R. Knight, M. E. Maxon, M. J. McFall-Ngai, J. F. Miller, K. S. Pollard, E. G. Ruby and S. A. Taha, A unified initiative to harness earth's microbiomes, *Science*, 2015, **350**, 507–508.

49 L. Lin, X. Peng, Z. Mao, W. Li, M. N. Yogeesh, B. B. Rajeeva, E. P. Perillo, A. K. Dunn, D. Akinwande and Y. Zheng, Bubble-pen lithography, *Nano Lett.*, 2016, **16**, 701–708.

50 E. C. Garnett, W. Cai, J. J. Cha, F. Mahmood, S. T. Connor, M. Greyson Christoforo, Y. Cui, M. D. McGehee and M. L. Brongersma, Self-limited plasmonic welding of silver nanowire junctions, *Nat. Mater.*, 2012, **11**, 241–249.

51 G. E. Jonsson, V. Miljkovic and A. Dmitriev, Nanoplasmon-enabled macroscopic thermal management, *Sci. Rep.*, 2014, **4**, 5111.

52 T. Uwada, S. Fujii, T. Sugiyama, A. Usman, A. Miura, H. Masuhara, K. Kanaizuka and M.-a. Haga, Glycine crystallization in solution by cw laser-induced microbubble on gold thin film surface, *ACS Appl. Mater. Interfaces*, 2012, **4**, 1158–1163.

53 K. Murayama and M. Tomida, Heat-induced secondary structure and conformation change of bovine serum albumin investigated by fourier transform infrared spectroscopy, *Biochemistry*, 2004, **43**, 11526–11532.

54 V. Militello, C. Casarino, A. Emanuele, A. Giostra, F. Pullara and M. Leone, Aggregation kinetics of bovine serum albumin studied by FTIR spectroscopy and light scattering, *Biophys. Chem.*, 2004, **107**, 175–187.